

## Trends in anomalous small-angle X-ray scattering in grazing incidence for supported nanoalloyed and core-shell metallic nanoparticles

P. Andreazza<sup>1,a</sup>, H. Khelfane<sup>1,2,3</sup>, O. Lyon<sup>4</sup>, C. Andreazza-Vignolle<sup>1</sup>, A.Y. Ramos<sup>5</sup>, and M. Samah<sup>2</sup>

<sup>1</sup> Centre de Recherche sur la Matière Divisée, UMR 6619 Université d'Orléans - CNRS, 1 bis, rue de la Férollerie, 45071 Orléans Cedex, France

<sup>2</sup> Laboratoire de Physique Théorique, Université A/MIRA, 06000 Bejaia, Algérie

<sup>3</sup> Faculté des Sciences, Université de Boumerdes, 35000 Boumerdes, Algérie

<sup>4</sup> Synchrotron Soleil, L'Orme de Merisiers, BP. 48, 91192 Gif-sur-Yvette, Cedex, France

<sup>5</sup> Institut Néel, CNRS et Université Joseph Fourier, BP. 166, 38042 Grenoble Cedex 9, France

Received 22 November 2011 / Received in final form 23 March 2012

Published online 15 June 2012

**Abstract.** As atomic structure and morphology of particles are directly correlated to their functional properties, experimental methods probing local and average features of particles at the nanoscale elicit a growing interest. Anomalous small-angle X-ray scattering (ASAXS) is a very attractive technique to investigate the size, shape and spatial distribution of nanoobjects embedded in a homogeneous matrix or in porous media. The anomalous variation of the scattering factor close to an absorption edge enables element specific investigations. In the case of supported nano-objects, the use of grazing incidence is necessary to limit the probed depth. The combination of grazing incidence with the anomalous technique provides a powerful new method, anomalous grazing incidence small-angle X-ray scattering (AGISAXS), to disentangle complex chemical patterns in supported multi-component nano-structures. Nevertheless, a proper data analysis requires accurate quantitative measurements associated to an adapted theoretical framework. This paper presents anomalous methods applied to nanoalloys phase separation in the 1–10 nm size range, and focuses on the application of AGISAXS in bimetallic systems: nanocomposite films and core-shell supported nanoparticles.

### 1 Introduction

Nanoscale metallic particles show peculiar chemical and physical properties intermediate between those of bulk metal and molecular clusters. These original properties

<sup>a</sup> e-mail: [Pascal.Andreazza@univ-orleans.fr](mailto:Pascal.Andreazza@univ-orleans.fr)

result from the large fraction of surface atoms and the finite size (3D confinement) effect in terms of electronic structure, magnetic moment, optical response, thermodynamic behavior, etc [1]. However they strongly depend on the type and chemical state of surface or interface atoms especially in the case of bimetallic nanoparticles (NPs). Compared to monometallic ones, the addition of one or several metals induces a larger diversity in their structure and morphology [2]. Besides the composition ( $A_xB_{1-x}$ ) effect, finite matter quantity effects lead to original variations of atom arrangement, such as disordered/ordered, segregated, core-shell and it should be noted that small size particle configurations are highly sensitive to kinetic and preparation factors. As physical and chemical properties are directly connected to atomic arrangement, it is then of primary importance to control the nanoalloys formation or evolution mechanisms. The capability to detect chemical order, disorder or demixion in nanomaterials, is a non-trivial issue [3–5], consequently the development of relevant methods to determine the size, shape, structural and chemical arrangements and spatial organization of NPs assemblies (nanocomposites, nanostructured films, supported particles) is still a key challenge.

Small-Angle X-ray Scattering (SAXS) is a well-established technique giving information on spatial correlation and morphological features of nanometric or submicroscopic objects [6,7]. The scattering intensity collected close to the X-ray incidence is directly related to large scale inhomogeneities in the electron density of the probed material. In complex materials, this intensity contains the contributions of the different scattering objects and/or the different parts of the object. These contributions can be disentangled using anomalous small angle X-ray scattering (ASAXS) [8–11]. ASAXS taking advantage of the variation of the scattering factor close to an absorption edge of a given element retrieves the specific contribution of this element [8,12,13]. For nano-objects supported on a dense substrate, SAXS and ASAXS methods, performed in transmission geometry, suffer from a lack of surface sensitivity due to a strong scattering contribution of the substrate or to a strong absorption of the particle scattering by the substrate. Grazing incidence geometry is compulsory to limit the probed depth. The combination of grazing incidence small-angle X-ray scattering with the anomalous technique (AGISAXS) provides a powerful method to extract the scattering data from multi-component supported nano-structures.

This paper presents some applications of ASAXS methods in nanoalloys phase separation (Sect. 2), then reports on recent original results of AGISAXS, applied to a system with two types of metallic particles and to supported core-shell CoPt nanoparticles (Sect. 3).

## 2 Anomalous small-angle X-ray scattering

The SAXS intensity is usually written as a function of the scattering vector  $\mathbf{q}$ , difference between the wave-vectors of incoming and scattered beam ( $|q| = 4\pi \sin(\theta)/\lambda$  where  $\lambda$  is the wavelength and  $2\theta$  is the scattering angle). For a multi-component material, where A and B atoms are present in a matrix m, a suitable expression is [14,15]:

$$I(\mathbf{q}, E) = \sum_{i,j=A,B} \Delta\rho_i \Delta\rho_j S_{ij}(\mathbf{q}) \quad (1)$$

where  $\Delta\rho_i = f_i/V_i - f_m/V_m$  is the electron-density contrast between the matrix and the metal i;  $V$  and  $f$  stand for the atomic volume and the scattering factor of a given element.  $S_{ij}(\mathbf{q})$  are the partial structure factors (PSFs) coming from the correlations between A atoms [ $S_{AA}(\mathbf{q})$ ], between B atoms [ $S_{BB}(\mathbf{q})$ ] and between A and B atoms [ $S_{AB}(\mathbf{q})$ ]. These factors express the scattering from the inhomogeneity induced by

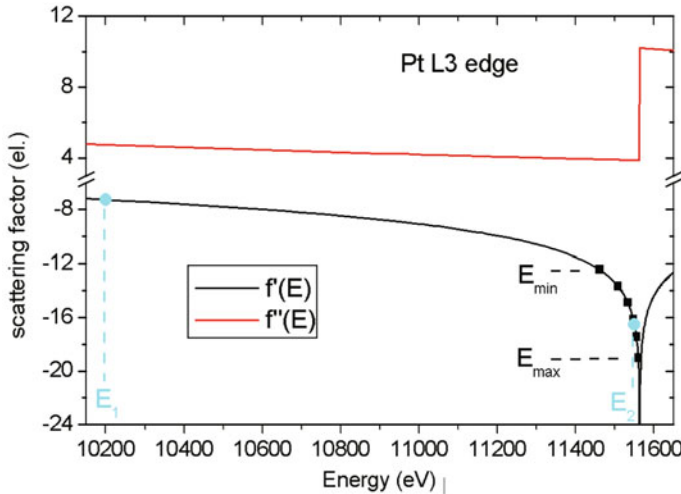


**Fig. 1.** Real  $f'$  and imaginary  $f''$  part of the scattering factor dispersion correction of a platinum atom in the vicinity of the L3-Pt absorption edge. Selected energies in the anomalous experiments described in Sect. 2.1 (full circles) and in Sect. 3.2 (squares).

A and B atoms with respect to the matrix (clustering) or by phase separation between A and B atoms and do not depend on the X-ray energy  $E$ . In the small angle conditions ( $q$  the scattering vector is close to zero) and far enough from its absorption edges, the scattering factor of a given element can be approximated by the atomic number  $Z$  of the element. This approximation is inappropriate when the X-ray energies  $E$  are adjusted near the absorption edge of the element. In this case, an anomalous dispersion correction is needed and the scattering factor is expressed by [16]:  $f(E) = Z + f'(E) + i f''(E)$  where  $f'$  and  $f''$  are, respectively, the real and imaginary part of the dispersion correction independent of  $q$  parameter, but strongly dependent on the X-ray energy [Fig. 1]. This energy dependence results in variations in the electron density contrast and consequently in the intensity scattered by the objects containing the selected element. As the partial structure factors keep constant as a function of  $E$ , the variation of the scattering intensities by varying  $E$  near the absorption edge of a given element makes possible the discrimination of the scattering entities containing this element.

Three scattering measurements at different energies provide *a priori* enough independent information to solve Eq. (1), and discriminate the scattering contribution from AA and BB pairs. In practice, the level of electronic contrast, the composition and the experimental conditions can simplify or complicate this discrimination. The analysis methods come within two types, referred as “direct method” and “differential method”. In the direct method, the intensities  $I(\mathbf{q}, E)$  measured at different energies are fitted directly with calculated models taking into account the variation of the scattering factor with energy. In the differential method, the partial structure factors are first extracted by difference between the intensities measured at different energies with various levels of approximation, then fitted with particle morphology models.

## 2.1 Monometallic particles in inhomogeneous matrix

A system of monometallic particles in an homogeneous matrix is described within the two-phase model, as randomly distributed scattering objects with sharp interfaces with the matrix: The scattering signal is only due to the particles. However, in most

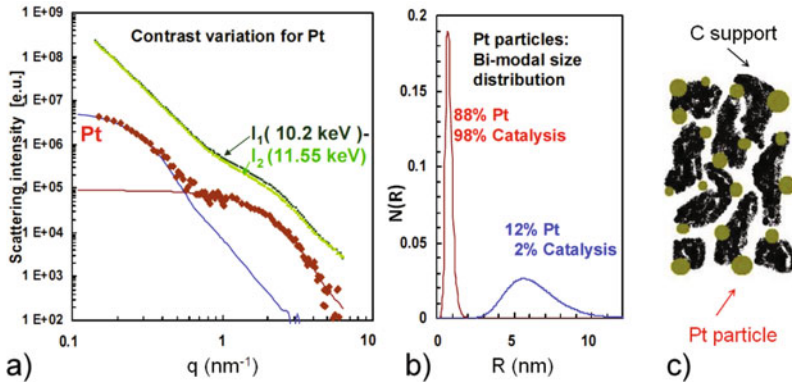


**Fig. 2.** Pt electrocatalyst particles in carbon supported fuel cell electrodes (From Haubold et al. [9]): (a) Scattering intensities  $I_1$ ,  $I_2$  for two X-ray energies with different scattering contrast (upper curves) and their difference with their best fits (lower curves) (b) bimodal log-normal size distribution (normalized for better view) deduced from these fits, (c) corresponding schematic drawing of this Pt-C nanocomposite.

real systems, the matrix exhibits density fluctuations (nanoporosity, defects, . . . ) contributing significantly to the total scattering signal. This is the case for metal catalyst particles in porous carbon support [9, 17–20]. As the carbon matrix is inhomogeneous, the system should be described using a three-phase model [21]. When the correlations between metal A and matrix m can be neglected, the scattering intensity is [Eq. (1)]:

$$I(\mathbf{q}, E) = |\Delta\rho_A(E)|^2 S_{AA}(\mathbf{q}) + |\Delta\rho_m|^2 S_m(\mathbf{q}) \quad (2)$$

where  $S_{AA}(\mathbf{q})$  is the particle contribution, while  $\Delta\rho_m$  and  $S_m(\mathbf{q})$  are the average electron density contrast and the scattering contribution of others scatterers in the matrix, respectively.

Figure 2 shows an example of ASAXS study of supported Pt catalyst particles in porous carbon electrodes as in electrical fuel cells. In this study from Haubold and coworkers [9], the strong anomalous effect near the Pt L3- absorption edge (see Fig. 1: two energies ( $E_2$ ) and ( $E_1$ ) were chosen near and far from the edge) was used to vary the scattering intensity due to the Pt catalyst, while the porosity scattering of the carbon support is almost energy independent in this energy range. The difference in the scattering intensities for these two X-ray energies then results from the catalyst particles alone [Fig. 2(a)], which can be treated as within a two-phase model. Considering an assembly of particles with a size distribution  $N(R)$  and a form factor  $F(q, R)$  corresponding to a spherical shape of  $R$  radius [22], the intensity from particles writes:

$$I_{part}(q) = |\Delta\rho_{part}(E)|^2 \int N(R) F(q, R)^2 S_{int}(q) dR \quad (3)$$

where  $S_{int}(q)$  is the interference function [6, 22] describing the spatial correlation between particles. When the assembly of particles is very diluted (low concentration) as in this example, the particles are uncorrelated and  $S_{int}(q) = 1$ . The ASAXS analysis reveals a bimodal log-normal function for Pt particles [Fig. 2(b–c)]: 88% of platinum atoms is dispersed in the form of small particles having a mean radii of 0.8 nm and 12% in larger particles. The weak surface-to-volume ratio of largest NPs induces only 2% of the catalysis reaction. This explains the non-optimized catalytic efficiency of this catalyst.

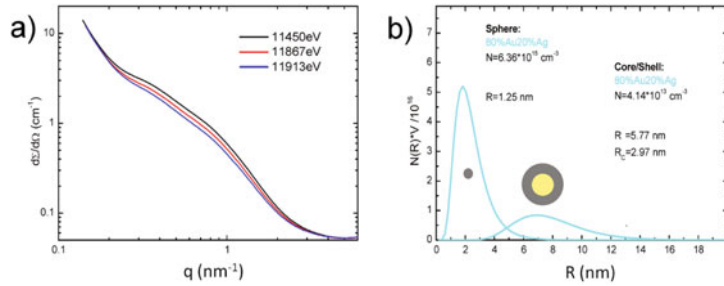


**Fig. 3.** Ag/Au nanoparticles in silica glass matrix (From Haug et al. [27]): (a) ASAXS patterns at three X-ray energies (11 450 eV, 11 867 eV, 11 913 eV) below the Au L3 edge, (b) deduced bimodal log-normal size distribution of alloyed small and core-shell large particles.

Similar ASAXS experiments can be performed *ex situ* or *in situ* during the formation of particles in solution or by thermal treatment. However, we should note the variations of the scattering factor in a range experimentally accessible are usually limited: from some % (K edges) to up 20% in the best cases (L edges). The anomalous variation of the intensity is then reduced and every correction for the primary beam intensity, detection sensitivity and deadtime must be carefully applied before any further data treatment. Particular attention must be taken to select an energy range fairly below the edge where the fluorescence background is constant with the energy. Otherwise, the used detector must provide an energy discrimination capability.

## 2.2 Core-shell bimetallic particles in matrix

When the particles keep the same morphology, but are made of two metals A and B randomly distributed inside the particle, the form factor remains unchanged. Only the average electron density contrast changes with the composition ( $A_xB_{1-x}$ ) with respect to pure particles. Matters turn more complicated for core-shell arrangement. The form factor of a heterogeneous particle of core radius  $R_c$  and shell thickness  $\Delta R$  becomes dependent on electron densities in the core and in the shell. The product  $|\Delta\rho_{part}(E)| F(q, R)$  in Eq. (3) is replaced by:

$$|\Delta\rho_{co}(E)| F_{co}(q, R_c) + |\Delta\rho_{sh}(E)| [F_{part}(q, R) - F_{co}(q, R_c)] \quad (4)$$

where  $\Delta\rho_{co}$  and  $\Delta\rho_{sh}$  are the average electron density contrasts in core and shell parts of the particle, respectively (defined with respect to dispersion media m, like vacuum, solvent, matrix).  $F_{part}(q, R)$  and  $F_{co}(q, R_c)$  are the form factor for a spherical scattering object of radius  $R$  for the whole particle and of a radius  $R_c$  for the core, respectively.

Only a limited number of papers are dedicated to investigations of core-shell particles by SAXS technique [23–25], and even less by ASAXS technique [19, 26, 27]. Figure 3 shows data extracted from recent works of Haug and coworkers [27]. These authors investigated the chemical composition and the morphology of nanosized bimetallic particles embedded in surface regions of a glass sample, prepared by double-ion implantation of Ag/Au. Preliminary transmission electron microscopy (TEM/HRTEM) observations showed two populations of NPs, the largest one exhibiting core-shell arrangement. ASAXS patterns were collected at three energies slightly below the Au L3 edge only. Due to the lack of information about the core and shell composition, the analysis proceeded in two steps. In a first step the ratios of the contrast between the three energies were fitted to obtain the composition of the small

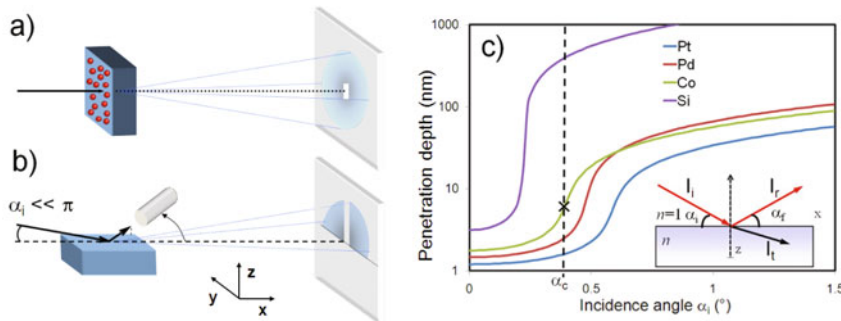


**Fig. 4.** Schematic drawing of the X-ray scattering geometry a) in transmission b) in grazing incidence for supported or included nanoparticles in a substrate; c) penetration depth versus incidence angle obtained at 8000 eV for Pt, Pd, Co and Si material. The total external reflection critical angle  $\alpha_c$  for cobalt is indicated by a dashed line.

spherical NPs and the shell of the core/shell NPs, without any regard on size distributions. The scattering contrast is then calculated and used in a second fitting step to retrieve all morphological parameters. For example in the sample of Fig. 3, the fitting analysis by the “direct method” gave the same composition in the small NPs and in the shell of the core/shell NPs [Fig. 3(b)]. The scattering contrast of the core was even smaller. This corresponds to an electron density smaller than that of pure Au or pure Ag. Therefore, the corresponding NPs should contain cores with either more or larger voids. More accurate information about the composition and density of these core/shell configurations would probably be obtained from combined ASAXS experiments at the two metal edges. We should note that in this complex case, the support of TEM observation was invaluable to provide a first set of morphological parameters.

Finally, as for TEM observations, the glass sample was polished to reduce its thickness to achieve acceptable transmission of X-rays. This experimental geometry appears unadapted to this kind of sample, where the particles are located in a region near the sample surface.

### 3 Anomalous grazing incidence small-angle X-ray scattering

X-ray scattering transmission geometry is commonly used for nanoparticles dispersed in the whole volume of a solvent, a colloid or a solid matrix. For a layer of particles on a substrate, the signal due to the nanoparticles is typically  $10^{-6}$  times weaker than spurious scattering due to the substrate. The signal to noise ratio for an experiment in the transmission geometry is then extremely low [Fig. 4(a)]. This ratio can be substantially improved in reflection mode using grazing incidence geometry [Fig. 4(b)]. By selecting an incidence angle  $\alpha_i$  on the sample surface close or even below the angle of total external reflection  $\alpha_c$  of X-rays (few tenths of degrees), the wave-field penetration depth can be decreased down to few nanometers. Thus, the surface or subsurface signal is enhanced with respect to the bulk [28]. The incident beam ( $I_i$ ) reflects in the specular direction ( $I_r$ ), and produces also a transmitted beam ( $I_t$ ) in the refractive direction in the material. The penetration depth of the X-rays can be tuned as a function of the incidence angle [Fig. 4(c)], close to the critical angle  $\alpha_c$  of total reflection. Any discontinuity in the local electronic density (surface roughness, islands, inclusions, etc.) scatters either the transmitted or the reflected beam.

Within the last years, grazing incidence small-angle X-ray scattering (GISAXS) emerged as a versatile technique in the field of nano-structured thin films and surfaces

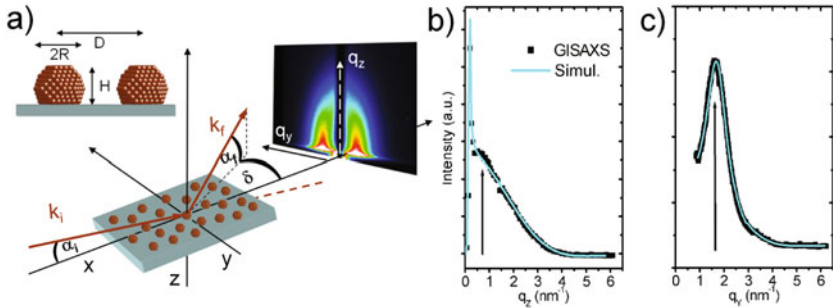


**Fig. 5.** a) 2D GISAXS pattern of alloyed deposited nanoparticles in the adapted GISAXS framework (from Andreazza et al. [3]). b) and c) at least, two cuts of intensity from the 2D pattern, in the  $q_y$  and  $q_z$  directions, selected in the lobe intensity region should be simultaneously fitted with dedicated codes [37–39], corresponding experimental (marks) and fits (line); the arrow shows the  $q$  position of the other perpendicular cut. The fit results give  $R = 1.0 \text{ nm}$ ,  $H = 1.5 \text{ nm}$  and  $\sigma(R)/R = 0.3$ .

[20, 29–33]. GISAXS is well adapted for the characterization of correlations and shape of objects at surfaces [34] or at buried interfaces [35]. Experimentally, the GISAXS intensity is recorded with a 2D detector mounted in an adapted framework [Fig. 5], as a function of the in-plane  $q_y$  and out-of-plane  $q_z$  components respectively parallel and perpendicular to the substrate [32, 36]. The 2D patterns reveal possible anisotropies of in-plane and out-of-plane organization and shape of nanoparticles. In the example of Fig. 5 corresponding to an assembly of supported alloyed CoPt NPs on silicon substrate, the form factor corresponds to a truncated quasi-spherical shape with a narrow size dispersion. Anisotropic form and structure factors are simultaneously fitted with calculated scattering profiles from at least two experimental cross sections (intensity cuts), in the  $q_y$  and  $q_z$  directions [Fig. 5(b-c)] [3]. Close to the total reflection conditions ( $\alpha_i \simeq \alpha_c$ ), the reflected intensity is strong enough to modify the small angle scattering intensity in shape and magnitude with respect to that obtained in a transmission measurement. Multiple scattering effects (among reflected and scattered beams) come into play [3, 33]. The kinematic approximation (Born approximation – BA) used in SAXS analysis becomes inadequate. The form factor should be described within the distorted wave Born approximation (DWBA) [28]. A strong enhancement of the intensity appears at  $\alpha_f = \alpha_c$  [Fig. 5(b)], referred as “the Yoneda peak”, originates from the interference of incoming and reflected beam. Consequently, the analysis of GISAXS patterns requires a formalism able to model the correlation and shape effects at grazing incidence. Two dedicated programs are available so far: IsGISAXS [37] restricted to nano-objects deposited on a substrate or arranged in a single particle layer (two dimensions) and FitGISAXS [38] more adapted to scattered objects arranged in two or three dimensions in a stratified medium.

The combination of GISAXS with the anomalous technique provides a powerful method to extract the scattering data from multi-component (several metals) supported nano-objects. This new technique, called “AGISAXS” has been recently used in order to demonstrate that the scattering from nanoparticles or islands on the surface of a substrate [40, 41] or within a layered matrix [42, 43] can be separated from that of the matrix, surface roughness and fluorescence. However quantitative analysis of anomalous measurements requires a very accurate monitoring of the incident intensity. At grazing incidence the beam footprint on the sample can be larger than the sample length and such monitoring is then a great experimental challenge. The proper data analysis requires then a computational combination of the specificities

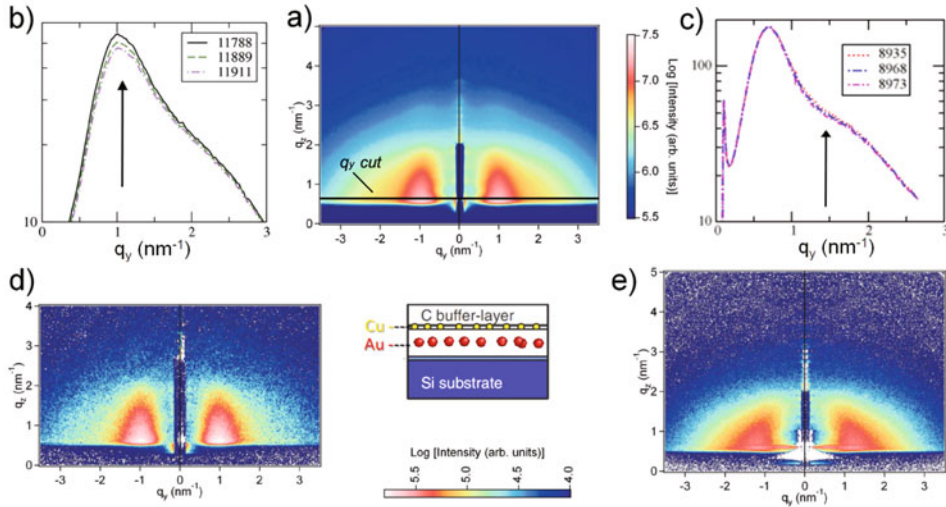


**Fig. 6.** (a) Average of the two-dimensional GISAXS patterns of the CCu/C/Au/C sample measured near the Cu K edge.  $q_y$  one-dimensional cross-sectional scans ( $q_y$  cuts at  $q_z = 0.7 \text{ nm}_1$ ) measured at different energies (eV) in the vicinity of the (b) Au L3 edge, and of the (c) Cu K edge. The arrows correspond to the zone of maximal anomalous Intensity variation. Two-dimensional differential GISAXS patterns calculated, (d) at 11911 eV with respect to the mean value near the Au L3 edge, and (e) at 8973 eV with respect to the mean value near the Cu K edge (From Simon et al. [43]).

of multi-scattering effects in grazing incidence and resonant anomalous effects in an adapted theoretical framework [33, 39].

### 3.1 Nanocomposite films

Anomalous GISAXS has been recently validated in the case of monometallic particles embedded in a carbon layer in a two phase model (one kind of metal particles) and in a three-phase model (two kinds of particles - metal A and metal B) by Simon et al. [43]. The samples were prepared to obtain separated copper particles or/and gold particles by a carbon buffer layer (see inset in Fig. 6). The scattering intensity contains copper and gold contributions. The carbon layers where the metallic particles were embedded, give additional scattering  $I_m(\mathbf{q})$  as in the catalyst particles in carbon matrix described in Sect. 2.2. In the case of uncorrelated scattering signals (between metal A, metal B and carbon layer), the GISAXS intensity of the CCu/C/Au/C nanocomposite film is given by:

$$I(\mathbf{q}, E) = |\Delta\rho_A(E)|^2 S_{partA}(\mathbf{q}) + |\Delta\rho_B(E)|^2 S_{partB}(\mathbf{q}) + I_m(\mathbf{q}). \quad (5)$$

The contributions of the intensity scattered by the Cu and Au nanoparticles and by the additional defects overlap, so that the GISAXS technique cannot distinguish between them. Typical patterns as in Fig. 6(a) display several lobes of intensity at different  $q_y$  positions corresponding to several scattering contributions. AGISAXS was used at the edges of the two metals. The corresponding one-dimensional profiles  $I(q, E)$  show up anomalous intensity variations at both the Au L3 [Fig. 6(b)] and Cu K edges [Fig. 6(c)] showing differences at different  $q_y$  positions. Fig. 6(d) and (e) present, respectively, the two-dimensional differential GISAXS patterns of

the CCu/C/Au/C sample calculated by differential method at 11911 eV with respect to the mean value near the Au L3 edge and at 8973 eV with respect to the mean value near the Cu K edge. The contributions of the Au and Cu nanoparticles are clearly separated: anomalous GISAXS at the Au L3 edge exclusively provides information on the Au NPs; and anomalous GISAXS at the Cu K edge exclusively provides information on the Cu NPs, since there is no correlation between the Cu and Au NPs. Then, quantitative analysis leads to determine the size distribution of copper and gold particles. Nevertheless, these results are less precise than in the binary samples (one metal particles and carbon layer) because the non-anomalous signal contributes to about half of the total intensity. Therefore, in order to differentiate the anomalous scattering of nanoparticles from the other types of scattering, their contribution to the GISAXS intensity should not be minor.

### 3.2 Core-shell and alloyed particles supported on a flat substrate

The core-shell structure provides a chemically- or magnetically-active coating around a metallic core for fuel cell and magnetic storage applications. The bimetallic system (Co,Pt) has a strong tendency for alloying, however under controlled synthesis conditions of the out-of equilibrium core-shell arrangement can be stabilized in the size range of 1–4 nm. We want to compare the morphology for NPs obtained by Co and Pt co-deposition and by sequentially-deposition of Co on the Pt-core. We used AGISAXS technique to address the question whether or not the out-of equilibrium core-shell arrangement is stable at room temperature and after annealing in NPs samples obtained by the two methods.

#### 3.2.1 Experimental and procedures

Co and Pt atoms were co-deposited or sequentially-deposited by condensation in UHV ( $3 \times 10^{-10}$  mbar) using electron beam evaporation on prepared amorphous SiO<sub>2</sub> layer on Si substrate [44]. The composition of the nanoparticles assembly is measured by an average method, the Rutherford backscattering (RBS) and a local method, the energy dispersive X-ray spectroscopy (EDX), in order to check the balance (+ – 5%) between Co and Pt atoms. The scattering experiments were performed at SWING beamline at the Synchrotron Facility SOLEIL (France) using a two-dimensional AVIEX CCD camera. The sample-detector distance was set to 1.2 m in order to optimize the q range of the data collection with respect to the particle size. As the anomalous effects are frequently low, it is necessary to properly correct the error sources in the data analysis. The main errors source are: the energy dependence of the detector counting efficiency, the typical dark count, the camera distortion, the variation of the beam footprint on the sample and the multiple interactions between reflected and scattering wave. The last two sources are minimized by choosing incidence angles,  $\alpha_i = 0.45$  and  $0.60^\circ$  for Pt L and Co K edges significantly larger than the critical angles of SiO<sub>2</sub> at these energies ( $\alpha_i = 0.16$  and  $0.23^\circ$ , respectively). For such  $\alpha_i$ , the beam footprint width is smaller than the sample length and the grazing incidence effects (including refraction, reflection and wave interactions) are fairly weak. Figure 7(a) displays the comparison between the calculated GISAXS patterns at two incidence values (close and far from the critical angle,  $\alpha_i = 0.2$  and  $0.6^\circ$  respectively) and the corresponding SAXS pattern at 11500 eV close to Pt L edge. The Yoneda peak excepted, the multi-scattering effects vanish at  $\alpha_i = 0.6^\circ$ . The intensity shape is close to the BA pattern. Consequently, variations in the GISAXS intensity are dominated by the anomalous contrast variations and we can use the “differential method”.

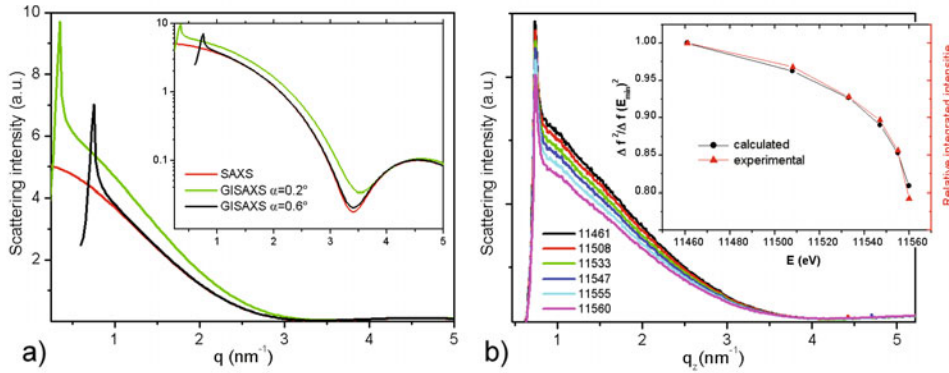


**Fig. 7.** (a) Calculated scattering patterns of a Pt-Co core-shell particle at two incidence values (close and far from the critical angle,  $\alpha_i = 0.2$  and  $0.6^\circ$  respectively) in GISAXS DWBA framework and in SAXS BA framework. The inset displays the same graph in logarithmic intensity scale. (b)  $q_z$  cuts of GISAXS patterns of Pt nanoparticles deposited on  $\text{SiO}_2$  at 6 energies just below the Pt L3 edge. The fit results give  $R = 1.2 \text{ nm}$ ,  $H = 1.7 \text{ nm}$  and  $\sigma(R)/R = 0.3$ . The inset shows the relative variation of integrated intensities with respect to the relative calculated contrast.

The experimental conditions and corrections were validated on a sample of Pt NPs. The measurements were performed at 6 energies close to the Pt L3 edge (from 11461 to 11560 eV) corresponding to a variation of 6.6 electrons for the scattering factor [Fig. 2]. Fig. 7(b) displays the out-of-plane  $q_z$  one-dimensional cuts obtained from 2D GISAXS patterns. As expected for monometallic particles, the profiles obtained for the different energies are homothetic and their intensity decreases as the X-ray energy increases. Integrated intensities are obtained by summations of the scattering intensity in the constant  $q$  range far from the Yoneda and beam stop region. Figure 7(b) shows the relative variations of these integrated intensities. They are identical within 2% to the curves calculated from theoretical values [16]. This outcome reveals that neither the substrate nor defects or heterogeneities give significant small angle scattering signal. In our system, the particles are barely supported on a homogeneous  $\text{SiO}_2$  layer covering a single crystalline substrate. The “matrix” can be considered as the vacuum.

### 3.2.2 Anomalous GISAXS results

The small angle scattering were measured at four energies at the vicinity of the Co K edge and the Pt L3 edge, corresponding to a scattering factor variation of 3.4 and 6.6 electrons respectively. The AGISAXS data at both edges were analyzed by the combination of the “differential method” and the “direct method”.

In a first step the evolution of the scattering intensity difference for the two edges provides a qualitative evaluation of the heterogeneity of the atomic arrangement of Pt and Co. For Co and Pt atoms randomly distributed in the particle, all partial scattering factors (Pt-Pt, Co-Pt and Co-Co) should be homothetic. On the other hand, anomalous effects can be expected in the case of core shell particles. In both cases, the interference function between particles, which describes the spatial organization of particles is the same for all PSFs [45].

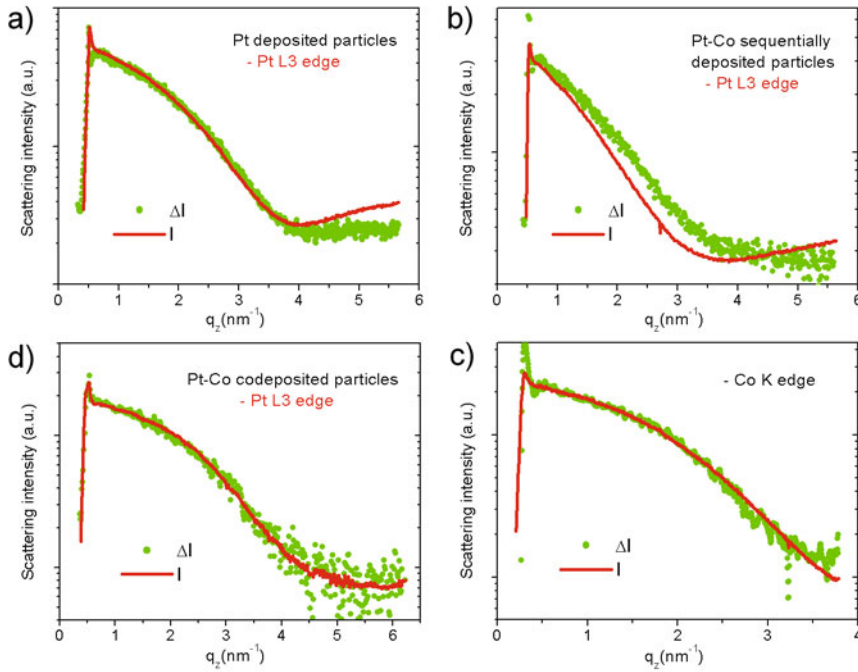


**Fig. 8.** GISAXS one-dimensional  $q_z$  cuts of (a) Pt nanoparticles alone, (b) and (c) Pt-Co sequentially deposited particles and (d) CoPt co-deposited particles at Pt L3 edge for a), b) and d) and at Co K edge for c). Differential intensity  $\Delta I = I(E_{max}) - I(E_{min})$  and total intensity  $I(E_{min})$  are showed for each graphs and  $\Delta I$  is normalized with respect to  $I(E_{min})$  to allow a direct comparison.

In both cases of core-shell or alloyed particles, the correlations  $[S_{ij}(\mathbf{q}) = S_{CoPt}(\mathbf{q})]$  term of eq. 1] between Co and Pt atoms are not negligible and the scattering intensity close to the absorption edge of the  $i$  atom ( $i = \text{Co}$  or  $\text{Pt}$ ) writes:

$$I(q, E) = |\Delta\rho_i(E)|^2 S_{ii}(q) + \Delta\rho_i(E)\Delta\rho_j S_{ij}(q) + |\Delta\rho_j|^2 S_{jj}(q). \quad (6)$$

Consequently, the difference of intensities between two energies varying below the absorption edge of the  $i$  atom contains two anomalous contributions: the  $S_{ii}(\mathbf{q})$  term and the  $S_{ij}(\mathbf{q})$  term. For example at the Pt L3 edge, the intensity difference becomes:

$$\Delta I(q, E_1, E_2) = I(q, E_1) - I(q, E_2) = \quad (7)$$

$$(|\Delta\rho_{Pt}(E_1)|^2 - |\Delta\rho_{Pt}(E_2)|^2)S_{PtPt}(q) + (\Delta\rho_{Pt}(E_1) - \Delta\rho_{Pt}(E_2))\Delta\rho_{Co}S_{CoPt}(q).$$

Fig. 8 shows the comparison between the out-of-plane scattering intensity from the entire particle and the difference  $\Delta I = I(E_{max}) - I(E_{min})$  for pure, sequentially deposited and co-deposited particles, where  $I(E_{max})$  and  $I(E_{min})$  are the energies 11461 and 11560 eV and 7606 and 7705 eV at the Pt L3 edge and at Co K edge, respectively [47]. The effect is significant at the edge of Pt core of sequentially deposited particles (Fig. 8(b)]. It reflects the size difference between the entire particle and the Pt “core”. Concerning the in-plane scattering intensities which contain mainly the interference function between particles, any significant difference is observed in the profiles (not shown here). These results confirm that growth kinetic traps

the core-shell structure for core Pt and shell Co sequentially deposited at room temperature, even if these two metals have a strong tendency to form an alloy. Similar measurements for CoPt co-deposited particles sample show homothetic profiles [only Pt edge results are showed in Fig. 8(d)] which confirm the alloying of bimetallic CoPt particles without segregation. We should note that we do not observed the same effect at the Co “shell” edge [Co K edge in Fig. 8(c)]. This can be explained by the high difference in the electron density between Pt and Co. At the Pt edge, the homogeneous term (Pt-Pt) in eq. 7 is dominant, while at the Co edge, the dominant term is the cross-correlation Co-Pt term with respect to the (Co-Co) term.

The GISAXS intensity of our assembly of supported particles can be expressed in the local monodisperse approximation as in eq. (3) with a form factor of nanoparticles calculated in the DWBA framework. NPs morphological parameters (radius  $R$ , height  $H$  and inter-particle distance) have been extracted from GISAXS experimental data by comparison with simulations using IsGISAXS software [37] (direct method). The best results are obtained with a spherical shape that can be truncated by the substrate surface by taking an aspect ratio  $H/2R < 1$ . A narrow Gaussian size distribution with relative geometrical standard deviation close to  $\sigma(R)/R = 0.3$  according to preliminary TEM observations is used for each simulation [46]. Based on the qualitative results of the differential method, several form factors were used: homogeneous truncated sphere for alloyed and pure particles and core-shell truncated sphere for sequentially deposited particles. This latter case corresponds to the sample of Fig. 8(b)–(c), and the analysis gives  $R = 1.4$  nm,  $H = 2.3$  nm for the entire particle and  $\Delta R = R - R_c = 0.35$  nm for the Co shell thickness. These results agree perfectly with a model of a Pt supported particle covered by a shell of two Co monolayers excepted at the substrate-Pt core interface. The atom number ratio between Pt and Co calculated with this model is in agreement with the atom quantity ratio obtained by RBS method over the whole sample or by EDX method at the scale of particles ( $N_{Pt}/N_{Co} = 3.3$ ). It corresponds to an average shell thickness of about 2 monolayers of Co. Further results, especially with PSF analysis method will be available in Ref. [47]. In the case of core-shell particle, the limit about the observation of the shell thickness remains to be determined. To our knowledge, anomalous scattering does not allow an accurate characterization of a core-shell arrangement below a shell thickness of 2 atom monolayers, even for two metals with high contrast.

## 4 Conclusion

Anomalous small-angle X-ray scattering (ASAXS) is a very attractive technique to investigate the size, shape and spatial distribution of nanoparticles (NPs) supported in porous media or embedded in homogeneous matrix. The anomalous effect – strong variation of the atomic factor close to an absorption edge – is used to discriminate the different intensity contributions of a multi-element nanostructured material. In the case of supported nano-objects, the use of grazing incidence is necessary to limit the probed depth and enhance the intensity coming from the supported inhomogeneities. The combination of grazing incidence small-angle X-ray scattering with the anomalous technique, provides a powerful new method, AGISAXS, to extract the scattering data from multi-component supported nano-structures. This paper reports on several applications of ASAXS methods in nanoalloys phase separation and recent original anomalous scattering results obtained using AGISAXS. It shows that a correct analysis of AGISAXS data requires accurate quantitative measurements associated to adapted theoretical framework and demonstrates the efficiency of AGISAXS

analysis applied to inhomogeneous nanostructured layers, provided a great care in the various steps of the data analysis.

During the formation of nanoparticles, the time and length scales of nucleation and growth processes and their inherent transient nature hind the possibility of simultaneous real time investigation at several energies. However, the combination of fast 2D detector, quick-monochromator and high brilliance of synchrotron radiation could enable the study of kinetic phenomena at intermediate time-interval of observation (above few seconds). The AGIXAXS technique could then provide new perspectives to investigate *in situ* and in real time the formation or the structural and morphological changes in nano-objects.

The authors are indebted to H.-G. Haubold, J. Haug and J.-P. Simon for providing the original material for the figures 2, 3 and 6, respectively. The authors also acknowledge the staff of SWING beamline of Synchrotron Soleil for technical assistance and J.-P. Simon and D. Babonneau for fruitfully contributions.

## References

1. D. Alloyeau, C. Mottet, C. Ricolleau, *Nanoalloys: Synthesis, Structure and Properties* (Springer-Verlag, London, 2011)
2. R. Ferrando, J. Jellinek, R.L. Johnston, Chem. Reviews **108**, 845 (2008)
3. P. Andreazza, C. Mottet, C. Andreazza-Vignolle, J. Penuelas, H.C.N. Tolentino M. De Santis, N. Bouet, R. Felici, Phys. Rev. B **82**, 155453 (2010)
4. D. Ferrer, D. Blom, L. Allard, S. Mejía, E. Pérez-Tijerina, M. José-Yacamán, J. Mat. Chem. **18**, 2442 (2008)
5. A.I. Frenkel, Zeit. Krystall. **222**, 605 (2007)
6. A. Guinier, G. Fournet, *Small-angle scattering of X-rays* (J. Wiley and Sons, 1955)
7. J.-P. Simon, J. Appl. Cryst. **40**, s1 (2007)
8. J.-P. Simon, O. Lyon, *Resonant Anomalous X-ray Scattering*, edited by G. Materlick, C.J. Sparks, K. Fischer (Elsevier Science, The Netherlands 1994), p. 305
9. H.-G. Haubold, P. Hiller, H. Jungbluth, T. Vad, Jpn. J. Appl. Phys. **38**, 36 (1999)
10. G. Goerigk, H.-G. Haubold, O. Lyon, J.-P. Simon, J. Appl. Cryst. **36**, 425 (2003)
11. U.-S. Jeng, Y.-H. Lai, H.-S. Sheu, J.-F. Lee, Y.-S. Sun, W.-T. Chuang, Y.-S. Huang, D.-G. Liu, J. Appl. Cryst. **40**, s418 (2007)
12. O. Lyon, J.J. Hoyt, R. Pro, B.E.C. Davis, B. Clark, D. de Fontaine, J.-P. Simon, J. Appl. Cryst. **18**, 480 (1985)
13. A. Ramos, O. Lyon, C. Levelut, J. Appl. Phys. **78**, 6916 (1995)
14. O. Lyon, J.P. Simon, Phys. Rev. B **35**, 5164 (1987)
15. G.J. Goerigk, D.L. Williamson J. Appl. Phys. **99**, 084309 (2006)
16. D. Creagh, J.H. Hubbell, S 4.2.4, D. Creagh, W.J. McAuley, S 4.2.6, in *International Tables for X-ray Crystallography*, vol. C, edited by A.J.C. Wilson (Kluwer Academic, Dordrecht, 1992)
17. F. Berg Rasmussen, A.M. Molenbroek, B.S. Clausen, R. Feidenhans, J. Catalysis **190**, 205 (2000)
18. T. Vad, H.-G. Haubold, N. Waldfner, H. Bonnemann, J. Appl. Cryst. **35**, 459 (2002)
19. C. Yu , S. Koh, J.E. Leisch, M.F. Toney, P. Strasser, Faraday Discuss. **140**, 283 (2008)
20. M. Mougenot, P. Andreazza, C. Andreazza-Vignolle, R. Escalier, Th. Sauvagec, O. Lyon, P. Brault, J. Nanopart. Res. **14**, 672 (2012)
21. H. Brumberger, D. Hagman, J. Goodisman, K.D. Finkelstein, J. Appl. Cryst. **38**, 147 (2005)
22. J.S. Pedersen, Adv. Colloid Interface Sci. **70**, 171 (1997)
23. J. Wagner, J. Appl. Cryst. **37**, 750 (2004)
24. O.O. Mykhaylyk, A.J. Ryan, N. Tzokova, N. Williams, J. Appl. Cryst. **40**, s506 (2007)

25. S. Seelenmeyera, I. Deikea, N. Dingenoutsa, S. Rosenfeldta, Ch. Norhausena, M. Ballauffa, T. Narayananb, J. Appl. Cryst. **33**, 574 (2000)
26. A. Hoell, F. Bley, A. Wiedemann, J.P. Simon, A. Mazuelas, P. Boesecke, Scripta Mater. **44**, 2335 (2001)
27. J. Haug, H. Kruth, M. Dubiel, H. Hofmeister, S. Haas, D. Tatchev, A. Hoell, Nanotechnology **20**, 505705 (2009)
28. J. Daillant, A. Gibaud, *X-ray and Neutron Reflectivity: Principle and Applications*, Lectures Notes in Physics (Springer-Verlag, London, 1999)
29. A. Naudon, D. Thiaudiere, J. Appl. Cryst. **30**, 822 (1997)
30. A.L. Thomann, P. Brault, J.P. Rozenbaum, C. Andreazza, P. Andreazza, H. Estrade, B. Rousseau, D. Babonneau, G. Blondiaux, J. Phys. D **30**, 3197 (1997)
31. P. Andreazza, C. Andreazza-Vignolle, J.P. Rozenbaum, A.L. Thomann, P. Brault, Surf. Coat. Technol. **151**, 122 (2002)
32. C. Revenant, F. Leroy, R. Lazzari, G. Renaud, C.R. Henry, Phys. Rev. B **69**, 035411 (2004)
33. G. Renaud, R. Lazzari, F. Leroy, Surf. Sci. Rep. **64**, 8, 255 (2009)
34. J. Penuelas, P. Andreazza, C. Andreazza-Vignolle, C. Mottet, M. De Santis, H.C.N. Tolentino, Eur. Phys. J. Special Topics **167**, 19 (2009)
35. D. Babonneau, G. Abadias, J. Toudert, T. Girardeau, E. Fonda, J.S. Micha, F. Petroff, J. Phys.: Condens. Matter **20**, 035218 (2008)
36. P. Andreazza, in *Nanoalloys: Synthesis, Structure and Properties*, edited by D. Alloyeau, C. Mottet, C. Ricolleau (Springer-Verlag, London, 2011)
37. R. Lazzari, J. Appl. Cryst. **35**, 406 (2002)
38. D. Babonneau, J. Appl. Cryst. **43**, 929 (2010)
39. O. Lyon, ActionJava software (2011)
40. B. Lee, S. Seifert, S.J. Riley, G.Y. Tikhonov, N.A. Tomczyk, S. Vajda, R.E. Winans, J. Chem. Phys. **123**, 074701 (2005)
41. F. Leroy, G. Renaud, A. Letoublon, R. Lazzari, Phys. Rev. B **77**, 235429 (2008)
42. T.-W. Huang, K.-L. Yu, Y.-F. Liao, C.-H. Lee, J. Appl. Cryst. **40**, s480 (2007)
43. J.-P. Simon, D. Babonneau, M. Drouet, O. Lyon, J. Appl. Cryst. **42**, 312 (2009)
44. J. Penuelas, C. Andreazza-Vignolle, P. Andreazza, A. Ouerghi, N. Bouet, Surf. Sci. **602**, 545 (2008)
45. F. Chassagneux, L. Bois, J.-P. Simon, C. Desroches and A. Brioude, J. Mater. Chem. **21**, 11947 (2011)
46. J. Penuelas, P. Andreazza, C. Andreazza-Vignolle, H.C.N. Tolentino, M. De Santis, C. Mottet, Phys. Rev. Lett. **100**, 115502 (2008)
47. H. Khelfane, P. Andreazza, C. Andreazza-Vignolle, O. Lyon, J. Penuelas, A. Ramos, Phys. Rev. B (to be published)